Master's Thesis of Landscape Architecture

High-temporal-spatial-resolution mapping for flood inundation using image fusion and decision tree

위성영상 융합과 의사결정나무를 이용한

홍수 침범 지역 지도화

February 2018

Graduate School of Seoul National University
Department of Landscape Architecture and Rural
Systems Engineering, Landscape Architecture Major

Jingrong Zhu

High-temporal-spatial-resolution mapping for flood inundation using image fusion and decision tree

Under the Direction of Adviser, Prof. Dong Kun Lee

Submitting a master's thesis of Landscape Architecture

February 2018

Graduate School of Seoul National University
Department of Landscape Architecture and Rural
Systems Engineering, Landscape Architecture Major

Jingrong Zhu

Confirming the master's thesis written by

Jingrong Zhu

February 2018

Chair   _____ (Seal)

Vice Chair   _____ (Seal)

Examiner   _____ (Seal)

Abstract

The mapping of spatial inundation patterns during flood events is important for environmental management and disaster monitoring. Satellite images provide important data sources for monitoring flood disasters. However, the trade-off between spatial and temporal resolutions of current satellite sensors limits their uses in flooding studies. This study applied data fusion models, the flexible spatiotemporal method, in generating synthetic flooding images with improved temporal and spatial resolution for flood mapping. This paper performs a detailed comparison of flood maps derived from for number of post-disaster prediction based on images acquired after the flooding, selected flood events in 2016 Tumen river in China. The result shows that the Landsat-like images generated can be successfully applied in flood mapping. From simulated Tumen river flood mapping during 29 August to 3 September,2016, can know when inundation occurs, this result map flood inundation region will full in map. Meanwhile, test the maximum inundation region and severely submerged spots and flood event occur and stop date during the event. The study suggests great potential of FSDAF in flooding research. Blending multi-sources images could also support other disaster studies that require remotely sensed data with both high spatial and temporal resolution.

Keyword: Flood inundation mapping, Landsat, MODIS, Decision Tree Model, Image fusion

Student Number: 2015-22382

Table of Contents

iii

Chapter 1. Introduction

1.1. Study Background

Flooding is a major hazard in both rural and urban areas worldwide with most severe impacts to the people and economics in the urban areas. Recent findings revealed that global warming induced heavy rainstorms have larger intensity than predicted / (Schiermeier, 2011; M. Faghih et al., 2017). This is especially true for areas where precipitation was heavy, for example, in the region broadly encompassing the Tumen river basin. It is found 648 mm (25.5 inches) of rain in the region from 20 to 31 August 2016. The intense precipitation was followed by inland and river flooding and in subsequent days produced additional backwater flooding. On 12 December, The United Nations Office on Humanitarian Affairs (OCHA) reported that 133 people were killed and 395 missing in North Hamkyung province in North Korea due to heavy rains and floods. More than 35,500 families have been injured with 69% completely destroyed, and 8,000 public buildings have been damaged. Accurate information on the extent of inundation is important for identify the area affected flood damage and to evaluate damage and flood prevention and management (Smith, 1997; Baumann, 1999). Also the spatial extent and temporal variation of flood-affected areas are required for flood hazard mitigation (Jung and Merwade, 2012;

Merwade et al., 2008).

Remotely sensed data can provide a spatially continuous and consistent map-like representation of the Earth's surface, and therefore, has been recognized as an important data source for seasonal water surface dynamics monitoring. This is especially true for the regions of inter regions where rivers and streams cross international boundaries as they they provide consistent and independently verifiable information (Brakenridge, R., & Anderson et al. 2006). Much effort had been devoted to record water dynamics from coarse-spatial-resolution satellite observations for flood mapping in many regions of the world (Sakamoto et al. 2007, Islam et al. 2010; Ticehurst et al. 2009). More recently, NASA has released a NASA Near Real Time Global Flood Mapping System, a fully automated, near real-time system designed to produce such products for nearly the entire globe each day by using MODIS data (Ahamed et al. 2017). However, a substantial proportion of water surface changes occur at resolutions below 250/500 m MODIS resolution. Therefore, coarse spatial resolution remote sensing data is not enough for catching the spatially detailed water surface changes information.

Landsat-like resolutions remote sensing data provide an alternative way for water surface dynamic mapping due to its 30m spatial resolution as well as its global acquisition strategy, long data record since 1972, reliable and consistently calibrated data record and continuing mission with future data availability (Wulder et al. 2016). Landsat images over multiple decades have been used to map seasonality and changes at continental and sub-

continental scales. However, in many regions, it is not easy to collect fine image (cloud cover<10%) of available images within a reasonable period (e.g., a season or a year) because of cloud contamination, Landsat 7 scan line corrector (SLC) off issue and incomplete spatial coverage of the global receiving stations required by sensors before Landsat-8 era (Wulder et al. 2016). Consequently, water related events that occur on shorter timescales, such as floods, may be missed. Seasonally flooded lands can also be drowned in the backwaters of new dams, while downstream fluvial systems become increasingly fragmented and desiccated; drowning, fragmentation and desiccation are all evident for many dammed rivers. Such information may not be retrieved using infrequent Landsat data.

1.2. Purpose of Research

However, the study using time series coarse resolution data to assist high resolution data mapping hydrological condition is rare. In this paper, we propose a method, Landsat data blended with time series MODIS data is investigated for improving spatial-temporal resolutions mapping water surface occur on shorter time scales. In this study, Tumen river down basin is selected as the study area as this is the borders of the three countries where collecting measurement data from multiple-national agencies can be very difficult or even worse that the administration paid less attention to and no data are collected on.

Chapter 2. Literature Review

2.1. Image fusion method

Existing spatiotemporal data fusion methods can be categorized into three groups: weighted function based, unmixing based, and dictionary-pair learning based. All of these methods need one or more observed pairs of coarse- and fine-resolution images for training and a coarse-resolution image at prediction date as input data. The output of these methods is a synthetic fine-resolution image at prediction date. Intrinsically, all spatiotemporal data fusion methods use spatial information from the input fine-resolution images and temporal information from the coarse-resolution images.

2.1.1 Weighted function based

Among the weighted function based methods, the spatial and temporal adaptive reflectance fusion model (STARFM) is the one developed first (Gao et al., 2006). STARFM assumes that changes of reflectance are consistent and comparable at coarse and fine resolutions if pixels in coarse-resolution images (hereafter referred to as "coarse pixels") are "pure" pixels,

in that one coarse pixel only includes one land cover type. In this case, changes derived from coarse pixels can be directly added to pixels in fine-resolution images (hereafter referred to as "fine pixels") to get the prediction. However, this ideal situation cannot be satisfied when coarse pixels are mixed, having a mixture of different land cover types. Therefore, STARFM predicts pixels with a function that gives a higher weight to purer coarse pixels based on information from neighboring fine pixels. STARFM was later modified and improved for more complex situations, resulting in the spatial temporal adaptive algorithm for mapping reflectance change (STAARCH), which improves STARFM's performance when land cover type change and disturbance exist (Hilker, Wulder, Coops, Linke, et al., 2009), and the Enhanced STARFM (ESTARFM), which improves STARFM's accuracy in heterogeneous areas (Zhu et al., 2010).

2.1.2 Unmixing based

Among the unmixing based methods, the multisensor multiresolution technique (MMT) proposed by Zhukov et al. (1999) is perhaps the first one to fuse images acquired at different times and with different resolutions. MMT has four steps to predict a fine-resolution image: (1) classify the input fine-resolution data to define endmembers at coarse resolution; (2) compute endmember fractions of each coarse pixel; (3) unmix the coarse pixels at the prediction date within a moving window; (4) assign unmixed reflectance to

fine pixels (Zhukov et al., 1999). In recent years, MMT has been modified by several studies to improve its accuracy. Zurita-Milla et al. (2008) introduced constraints into the linear unmixing process to ensure that the solved reflectance values were positive and within an appropriate range. Wu et al. (2012) estimated re-flectance change through unmixing endmember reflectance at both input and prediction date and then added the estimated change back to the base fine-resolution image to get the prediction. Amorós-López et al. (2013) modified the cost function to prevent the solved endmember reflectance from being greatly different from a predefined endmember reflectance. Gevaert and García-Haro(2015) directly unmixed the change of coarse pixels to estimate the change of endmembers and applied Bayesian theory to constrain the estimation.

2.1.3 Dictionary-pair learning based

Compared with weighted function and unmixing based methods, dictionary-pair learning based spatiotemporal data fusion methods are relatively new. Dictionary-pair learning based algorithms establish correspondences between fine- and coarse-resolution images based on their structural similarity, which can be used to capture the main features, including land cover type changes, in the predictions. The Sparse-representation-based SpatioTemporal reflectance Fusion Model (SPSTFM) is perhaps the first to bring dictionary-pair learning techniques from natural

image superresolution to spatiotemporal data fusion (Huang & Song, 2012). SPSTFM establishes a correspondence between the change of two fine-resolution images and two coarseresolution images through dictionary-pair learning, and then the trained dictionary is applied to predict a high-resolution image at the prediction date. Following SPSTFM, Song and Huang (2013) developed another dictionary-pair learning based fusion method which uses only one pair of fine- and coarse-resolution images. This method trains a dictionary pair on the input fine- and coarse-resolution image pair, and then downscales the coarse-resolution image at the prediction date by a sparse coding technique. Due to the large scale difference between MODIS and Landsat, this method is implemented in a two-layer framework, i.e., it first predicts an image with a middle-resolution between the fine- and coarse-resolution and then predicts the fine-resolution image based on the middle-resolution image (Song & Huang, 2013).

2.1.4 Flexible Spatiotemporal Data Fusion (FSDAF)

FSDAF refines the selected purest coarse pixels to avoid the effects of land cover type change on temporal change estimation. Existing unmixing based methods use endmember fractions obtained directly from the input fine-resolution image, assuming no land cover type change between the input image and the prediction date. However, this assumption may be not valid in areas with frequent disturbance or land cover type change, or a long time interval between input and prediction dates. If no land cover type

change happens, the temporal change of selected purest coarse pixels for each endmember should be similar to each other. In addition, pixels with land cover type change are often rare compared with the no-change pixels in an image. Therefore, it is reasonable to use quantiles to exclude coarse pixels with probable land cover type change based on their relative abundance. Second, local variability of temporal change caused by land cover conversions or within-class differences is modeled well through the distribution of residuals. STARFM and unmixing based methods estimate reflectance change within a moving window to account for withinclass differences. However, this moving-window strategy leads to inaccurate estimates in highly mixed landscapes in STARFM and unrealistic solutions for pixels with high correlation in unmixing based methods. In addition, these methods do not consider land cover type change. The proposed method decomposes the total change of each fine pixel into global change and local change. The local change, including both within-class differences and land cover type change, is estimated through distribution of the residuals from the temporal prediction. Because the coarse-resolution image is the only available information showing the situation at the prediction date, it is used to guide the distribution of residuals. Assuming both within-class differences and land cover type change have spatial dependence, FSDAF applies the TPS method to downscale the coarse-resolution image at the prediction date to fine resolution. The downscaled image can help us to judge which pixels have land cover type change or within-class variance so that we can better distribute residuals. Third, FSDAF predicts images with good spatial continuity through bringing in neighborhood information. This

strategy has been used in STARFM and STARFM-like methods but never in unmixing based methods. Current unmixing based methods are implemented one coarse pixel at a time.

As a result, FSDAF needs nearly equal time as STARFM even though it has more steps. For unmixing based methods, most computing time is used to invert the linear equation system to obtain endmember values at fine resolution for each coarse pixel. In contrast, FSDAF only needs to invert the linear equation system one time, because it uses global change values of endmembers. Therefore, FSDAF only needs about one third more processing time than unmixing based methods despite its additional steps.

2.2 Flood mapping

Many studies have been conducted using remote-sensing data to detect spatial and temporal changes in the extent of the flood inundation (Martineza et al., 2007; Sahoo et al., 2006; Hossain et al., 2007).

2.2.1 Pixel based classification

Traditional pixel-based image analysis algorithms for flood mapping and land use classification suffer from low accuracy, sub-pixel problems, and the speckle noise effect in the resulting images.

2.2.2 Object-based classification

On the other hand, the object-based image analysis (OBIA) approach has been thoroughly developed in the last two decades to overcome the limitations and disadvantages of the traditional pixel-based approaches by generating and analyzing meaningful image objects instead of individual pixels and reducing the speckle noise effect. The OBIA approach is conducted through a two-step process: (1) image segmentation by aggregating a number of individual pixels or image sub-objects to form larger objects (primitive objects) based on the homogeneity, intensity, and texture of each investigated image; and (2) image classification and feature extraction. The result of the OBIA approach was successfully proved to be more accurate than that of the pixel-based approaches for land cover classification in recent studies, such as discrimination of different species of mangroves with Worldview-2 imagery, flood area delineation in the trans-boundary areas using the ENVISAT/ASAR and Landsat TM data, and crop mapping using the multi-temporal Landsat imagery. Other applications of the object-based method for flood water and inundation mapping were introduced in. The object-based approach is normally used for the high spatial resolution images with a pixel size smaller than those of the objects of interest. The application of this method for the coarse resolution imagery is less common as the pixel size is larger than the object, and the image can be under-segmented. However, the image segmentation can be employed at

different resolutions to create homogeneous regions based on spatial and spectral information for identifying various objects at different scales and sizes can be detected as deviations from DCT trajectories. Delineation of dynamic classes may benefit from data transformations that accentuate both prevalent types of surface cover and key transitions (Cattell and Murphy, 1973; Neeti and Eastman, 2014). It may be also useful to map DCTs with object-based image analysis (OBIA) where prior to classification, image pixels are segmented into "objects" matching spatial entities (Dronova et al., 2011; Dronova et al., 2012). Even small "primitive" objects have been shown to improve classification accuracy relative to pixels by smoothing local noise and enhancing class contrasts with non-spectral attributes (Conchedda et al., 2008; Grenier et al., 2007; Kim et al., 2011). Using prior knowledge to define DCTs may facilitate differentiating among short-term variation for the processes of interest, while novel change or sporadic disturbances.

2.2.3 Decision Tree

Traditional mapping approaches have often focused on static classes representing discrete states of surface cover observable for extended periods of time. The "change" is assumed to occur for a given location if the highest-probability cover classes differ among successive points in time, and various change detection techniques have been summarized in several

reviews (Coppin et al., 2004; Gong and Xu, 2003; Lu et al., 2004; Mas, 1999). However, both classification and change detection are challenging in rapidly varying areas such as periodically inundated wetlands, where short-term surface dynamics produce transitional states and fine-scale mixtures of classes and may obscure long-term surface trends.

Decision tree analysis (DTA) is a rule-based technique that has produced highly accurate classifications based on a variety of spectral and ancillary data sources (Lawrence et al. 2004). Similar to neural networks, DTA is a non-parametric technique that does not assume normal distributions in the available datasets. DTA forms dichotomous decision trees using continuous or categorical data (Lawrence et al. 2004). The DTA algorithm works to reduce both intra-class and inter-class variability through recursive binary splitting of training data values (Venables and Ripley 1997). The results of such binary splits are displayed as branching dichotomous trees that serve as readily interpretable illustrations of variability within the data. Splits are applied to the classification of an image through classification rules (Lawrence and Wright 2001). Combinations of multispectral and ancillary data have been used in decision trees to produce highly accurate land-cover classifications. Decision trees are easily interpreted and can provide valuable insight into ecological conditions.

Recent refinements of decision tree approaches can result in more accurate classifications, albeit easily interpretable classification rules are often sacrificed when using more complicated refinements. Since decision trees are formed using a one-step-look-ahead, initial splits to reduce the

greatest variability largely determine the effectiveness of the tree to distinguish more detailed separations further down the tree (Venables and Ripley 1997, Lawrence et al. 2004). Less effective splitting occurs when outliers are present in the data or when attempting to classify land cover containing high within-class variability. Additionally, if the class of interest represents a small portion of the landscape and the training data are collected in similar proportions, the less dominant land-cover types can be under-classified with decision tree (Lawrence et al. 2004). These issues are applicable to wetland classification within a large landscape and thus encouraged a closer examination as part of our analysis.

Chapter 3. Materials and Methods

3.1. Study Area

The study area is located in the mid-western part of Tumen river basion, China (42°30′N 130°40′E). It is on the border of China, Russia and North Korea by the western coast of Japanese Sea. The 900×900 ㎡ area covers the majority of Hunchun, this study area has a heterogeneous landscape, including water bodies, vegetation, and urban land. The region experienced a devastating flood event was found 648 mm (25.5 inches) of rain in the region from 29 to 31 August 2016. The intense precipitation was followed by inland and river flooding and in subsequent days produced additional backwater flooding. According to the statistics obtained from United Nations Office on Humanitarian Affairs (OCHA) for 133 people were killed and 395 missing in North Hamkyung province in North Korea due to heavy rains and floods. More than 35,500 families have been injured with 69% completely destroyed, and 8,000 public buildings have been damaged. It contains the city of Hunchun, Jilin, China and the adjacent areas where the River Tumen goes through. It has a typical marine climate with an annual average temperature of 5–6°C. Many natural and artificial oases are distributed along the Tumen River watershed, most of which have been

converted into farming lands.
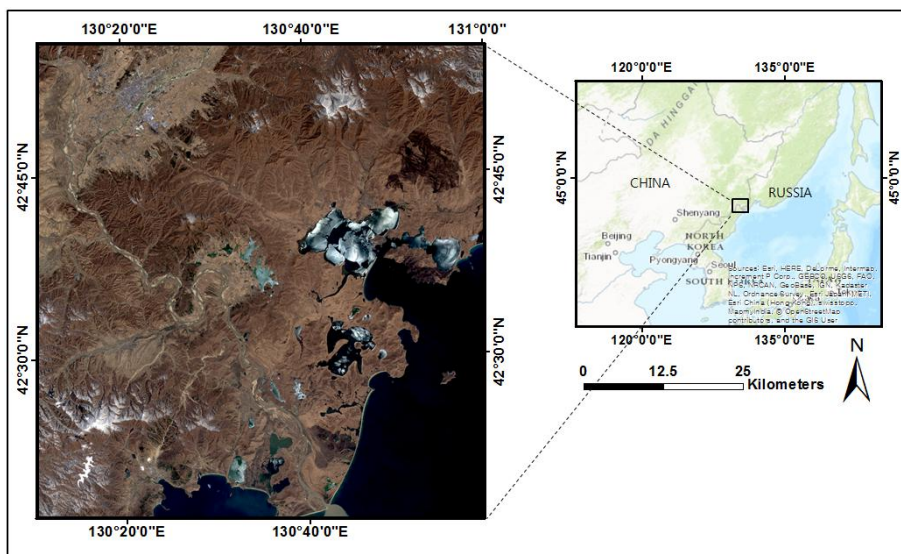
Figure 1 Study area with Tumen river basin and sampling sites marked on the Landsat 8

OLI image (RGB) from 25 March, 2016.

3.2 Material and Methods

3.2.1 Satellite Images and Data Processing

FSDAF use multiple Landsat and MODIS images as inputs to generate a 30 m Landsat-like image. While FSDAF needs one such MODIS image and at least one such Landsat–MODIS pairs. In this study, one pair of cloud-free Landsat images and MODIS surface reflectance products were collected to test the performance of FSDAF.

Two Landsat images (acquired on 6 July 2015, 16 August 2016) were downloaded from USGS. Each image was calibrated to reflectance to make it comparable with the MODIS products. All these data are of high quality. For the same period as the Landsat data, daily, 500 m MODIS nadir bidirectional reflectance distribution function (BRDF) adjusted reflectance datasets (MCD43A4), were acquired from the NASA Land Processes Distributed Active Archive Center (LPDAAC) (Figure 2). The reason why used 16-day composite MODIS data rather than MODIS daily data in Tumen river is because of the persistent cloud contamination in the latter product. In contrast, 16-day composite MODIS product can provide a much clearer view of the study area, and it is also proven to be able to generate better synthetic images by blending methods (Liu and Weng 2012). MCD43A4 is a 16-day rolling composite, representing the best BRDF possible during this period of time. Unlike in the previous collection 5, the date associated with each daily dataset is the center of the moving 16-day input window (and not its first day). In summary, the six MODIS were collected during the flooding in August 29, 2016 to September 3, 2016, were used in test Tumen river flood inundation time and maximum inundation boundary. The two Landsat data images in this one (acquired on 6 July 2015) was used as FSDAF model input data, other one (acquired on 16 August 2016) is a reference to assess the accuracy of the FSDAF model.

In this study assembled clear (10% cloud cover) Landsat-8 OLI scenes for the study area throughout the year 2016. Since the MODIS uses the same radiative transfer model for its atmospheric correction algorithm, this

paper used the Landsat Ecosystem Disturbance Adaptive Processing System (LEDAPS) to calibrated and atmospherically correct each scene.

Table 1 Characteristics of the satellite image utilized in the study.

Image data	Satellite	
	Landsat8 OLI	MCD43A4
Acquisition date	20160325	20160325 20160829 20160830 20160831 20160901 20160902 20160903
Part of the study area image	900*900	900*900
Nadir angle(degrees)	nd	
Format delivery	CEOS	HDF-EOS
Spectral range used	1,2,3,4,5,7	1,2,3,4,5,7
Spatial resolution(m)	30	500
Cloud cover(%)	0%	0%
Area of original scene(km²)	180*180	2400*2400

3.2.1.1 Landsat-8 Operational Land Imager (OLI)

FSDAF algorithm uses one pair same date Landsat and MODIS images and FSDAF needs one MODIS image on the flooding day studied as inputs to generate a 30 m Landsat-like image. In this study, one pair of cloud-free

Landsat images and MODIS surface reflectance products were collected to test the performance of FSDAF. Each image was calibrated to reflectance to make it comparable with the MODIS product. Eight 500 m, 8-day composite surface reflectance MODIS data sets, were acquired from the NASA Land Processes Distributed Active Archive Center (LPDAAC) (Figure 2). We assembled clear (10% cloud cover) Landsat-8 OLI scenes for the study area throughout the year 2016. Scenes were acquired using the USGS GLOVIS portal (http://glovis.usgs.gov). Since the MODIS uses the same radiative transfer model for its atmospheric correction algorithm, this paper used the Landsat Ecosystem Disturbance Adaptive Processing System (LEDAPS) to calibrated and atmospherically correct each scene.

3.2.1.2 Terra/Aqua Moderate Resolution Imaging S pectroradiometer (MODIS) MCD43A4, Colle ction 6

For the same period as the Landsat data, daily, 500 m MODIS nadir bidirectional reflectance distribution function (BRDF) adjusted reflectance datasets (MCD43A4). A major improvement of MCD43A4 collection 6 is that the production frequency has been increased from 8 days to daily, providing maximum flexibility in the definition of dates and time steps for generation of high temporal resolution time series with FSDAF. MCD43A4 is a 16-day rolling composite, representing the best BRDF possible during the periods of time. Unlike in the previous collection 5, the date associated

with each daily dataset is the center of the moving 16-day input window (and not its first day). More information on collection 6 of the MCD43A4 product can be found in the MODIS User Guide. The red and NIR bands of the MODIS datasets have been resampled using the nearest neighbor method to a resolution of 30 m, automatically co-registered to Landsat, and re-projected to UTM zone 30|N using the MODIS Reprojection Tool (MRT).

To run the FSDAF algorithms, all the input data need to have the same coordinate system and spatial resolution. Therefore, the MODIS data were first reprojected to UTM projection using USGS MODIS Reprojection Tool (MRT). Then, as the study area is on the boundaries of two MODIS tiles, the mosaic is needed for the two adjacent MODIS scenes obtained on the same day. ENVI software version 4.8 is used to resample the mosaic MODIS data to 30 m spatial resolution, then geo-reference it to the Landsat scene, and finally crop it to the size of the Landsat image.

3.2.2 Predicting flooding images through FSDAF and accuracy assessment

FSDAF produces a synthetic image from one pair of Landsat image and Modis images acquired on the same day (Tb) and one or more MODIS observations from the prediction date (Tn). FSDAF includes six main steps: (1) classify the Landsat image at Tb; (2) estimate the temporal change of each class in the MODIS image from Tb to Tn; (3) predict the Landsat

image at Tn using the class-level temporal change and calculate residuals at each MODIS pixel; (4) predict the Landsat image from the MODIS image at Tn with a Thin Plate Spline (TPS) interpolator; (5) distribute residuals based on TPS prediction; and (6) get the Landsat image of the Landsat image using information in the neighborhood. MODIS and Landsat surface data are very consistent relative to one another (Zhu et al., 2016), but variations exist due to bandwidth and solar geometry differences. For each MODIS pixel, its value is equal to the sum of values of all Landsat pixels inside it and a bias factor ξ which is the system difference between two sensors caused by differences in bandwidth and solar geometry. The high consistency of MODIS and Landsat surface reflectance data allows the premise that

$$M_b\left(x_i,y_i,\mathrm{B}\right) = \frac{1}{m}\sum_{j=1} L_b\left(x_{ij},y_{ij},\mathrm{B}\right) + \delta \qquad \mathrm{Eq.(1)}$$

where L_b and M_b represent the Landsat and MODIS surface reflectances, respectively, at a given pixel location $\left(x_i,y_i,\mathrm{B}\right)$ and acquisition date Tb, and is the difference between the observed Landsat and MODIS reflectances. where R is the between the Landsat pixels values and temporal prediction of Landsat ($\mathrm{Landsat}_b$) pixels. From Eq. (2) can see that distributing residual R (xi, yi, b) to Landsat pixels within a Modis pixel is a key step to improve the accuracy of temporal prediction of fine pixel value at Tn.

$$R\left(x_i,y_i,\mathrm{B}\right) = \Delta M\left(x_i,y_i,\mathrm{B}\right) - \left[\frac{1}{m}\sum_{j=1}^{m} L_n^{TP}\left(x_{ij},y_{ij},\mathrm{B}\right) - \sum_{j=1}^{m} L_b\left(x_{ij},y_{ij},\mathrm{B}\right)\right]$$
$$\mathrm{Eq.(2)}$$

If these differences remain consistent across time such that R=0 on a date Tn for which MODIS data are available but Landsat data are unavailable. The intrusion of various factors (i.e., mixed land cover types, land cover and phenology changes, and BRDF effects) estimate the temporal change of each class that are more homogeneous, spatially closer, and show less spectral reflectance change between the acquisition dates are same image (Zhu et al., 2016). This will effect on classify flood inundation extent.

The August 16,2016 images predicted by FSDAF methods were compared with the true images quantitatively and visually. Several indices were calculated to represent different aspects of accuracy. Root mean square error (RMSE) was used to gauge the difference between the predicted reflectance and the actual reflectance. Correlation coefficient r was used to show the linear relationship between predicted and actual reflectance. Average difference (AD) between predicted and true images was used to represent the overall bias of predictions. Positive AD indicates that the fused image generally overestimates the actual values, while negative AD means underestimation. Besides the above quantitative assessment, a visual assessment index, structure similarity (SSIM) (Wang, Bovik, Sheikh, & Simoncelli, 2004), was also used to evaluate the similarity of the overall structure between the true and predicted images:

$$\text{SSIM} = \frac{(2\mu_x\mu_y + C_1)(2\sigma_{xy} + C_2)}{(\mu_x^2 + \mu_y^2 + C_1)(\sigma_x + \sigma_y + C_2)} \qquad \text{Eq.(3)}$$

where μX and μY are means, σX and σY are variance of true and

predicted images, σXY is the covariance of the two images, C1 and C2 are two small constants to avoid unstable results when the denominator of Eq. (3) is very close to zero. A SSIM value closer to 1 indicates more similarity between the two images. To better demonstrate the effectiveness of data fusion methods, these four accuracy indices were also calculated between the actual fine-resolution image at prediction time and the input fine-resolution image. Indices from two actual fine-resolution images were used as baseline to evaluate whether data fusion methods can add correct temporal information to the input fine-resolution image. Images produced by spatiotemporal data fusion methods have various applications (Emelyanova et al., 2013).

Land cover classification is one important application of these fused images. To evaluate whether or not FSDAF can benefit the further applications, classified the original Landsat image and all predicted images of the site experienced a large flood during August 29 to 3 September,2016 to get land cover maps. To exclude effects from other factors, the study applied the same classifier, i.e., support vector machine (SVM), and the same set of training data to all images. These images were classified into vegetation, low vegetation, inundated land, and water. The classification map of original Landsat image was used as reference map to quantitatively assess the agreement between it and other classification maps of predicted images by error matrix (Liu, Frazier, & Kumar, 2007). Overall accuracy (oa) and kappa coefficient derived from error matrix were reported to evaluate the agreement at map level. For the category level, the average value of

user's and producer's accuracy (aup) was used to assess the agreement of each class (Liu et al., 2007).

3.2.3 Flood mapping and accuracy assessment

Remote sensing classifications of this area from single-date images exhibit high uncertainty due to complex flood inundation and frequent transitional mixtures of classes (Dronova et al., 2011). Complex surface composition and dynamics may result in large number of detected unique change pathways, some of which may not be physically plausible (Hess et al., 2003; Liu and Cai, 2011; Villa et al., 2012), representing error and noise (Mc Cleary et al., 2008).

DT is developed to find the optimal hyperplane to separate two classes, flooding and non-flooding classes in this case, while maximizing the margin between the closest points in different classes (Cortes and Vapnik 1995). It is widely used in classification and proven to be competitive with many other classic learning algorithms (Huang, Davis, and Townshend 2002). The pixels which can be correctly identified as inundated or non-inundated by visual interpretation are selected as training samples. Using the same training samples, an inundation map will be produced from each of the predicted images as well as the actual image of the predicted day that is regarded as the flooding reference map. Although this flooding reference map is not the ground truth, the actual Landsat data classified using the

same training samples and classifier can be an appropriate baseline to evaluate the effectiveness of these blending methods in flood mapping.

The algorithm used by the Sakamoto et al. (2007) was modified in this study. The previous algorithms used by Sakamoto et al. (2007) were examined and some components were excluded from the algorithm used here. In the previous algorithm, a wavelet-based filter was used to smooth data by removing the noise component and interpolating for any missing information. As a result, this algorithm creates artificial data and was not used in this study. The production of inundation maps in this study used a decision tree to associate each pixel with one of the following categories: the flood, mixed, nonflood and water related pixels. The decision tree is illustrated in Figure n and may be summarized as follows:

The first step was to detect cloud cover pixels from the image. If blue reflectance (band 3 of MODIS) is equal to or 40.2 (Thenkabail et al., 2005; Xiao et al., 2006), it is considered as a cloudy pixel. Using this formula, the data related to cloudy pixels were removed from the image. The next step was to estimate MNDWI, LSWI and the difference value of MNDWI and LSWI, DVEL for each of the land class cover types. In this study, the discrimination of water-related pixels and non-flood pixels was conducted in accordance with the pioneering method developed by Xiao et al. (2005, 2006). The MNDWI, LSWI and DVEL are used exclusively to discriminate between the flood, mixed, non-flood and water-related pixels. The changes in MNDVI, LSI and DVEL for different land use types are shown for 2007 in Figure n. If the MNDWI is 40.3, it can be classified as a non-flood related

pixel.

The MNDWI of permanent water bodies such as 'River' and 'Sea' land-use types are >0.05 or even show negative values throughout the year. The DVEL of 'River' and 'Sea' land-use types have a DVEL value >0.05. It can be inferred that water-related pixels should have a DVEL of >0.05. However, excluding the 'Lake' land-use type, the DVEL value is not always >0.05. To overcome this problem, another criterion is used to identify water-related pixels. In such cases, if the MNDWI is –0.05 and the LSWI is 0, the pixel will be identified as a water-related pixel. After identifying the water-related pixels, it is essential to classify whether it is a flood pixel, a long-term water body or a mixed-type pixel. Because of the moderate-resolution (30m) sensor of Landsat, a pixel can be composed of a mixture of different types of land surfaces. It is difficult to discriminate between vegetation mixed with water and vegetation completely flooded by water. Figure n shows that the MNDWI is of 'Sea', 'Lake' or 'River' land types are below 0.1 and, as a result, this criterion can be used for a further classification of the water-related pixels. If a water-related pixel has an MNDWI of >0.1, it will be considered as a flood pixel. If the MNDWI is 40.1 but >0.3, it will be identified as a mixed pixel. Finally, areas that are inundated throughout the year should be separated from the flood and mixed pixels. Many of the water bodies in Tumen river have been identified as inundated, such as small wetlands known as 'Beels' and large wetlands are known as 'Haors'.

DT is developed to find the optimal hyperplane to separate two classes, flooding and non-flooding classes in this case, while maximizing the margin

between the closest points in different classes (Cortes and Vapnik 1995). It is widely used in classification and proven to be competitive with many other classic learning algorithms (Huang, Davis, and Townshend 2002). The pixels which can be correctly identified as inundated or non-inundated by the method are selected as training samples. Using the same training samples, an inundation map will be produced from each of the predicted images as well as the actual image of the predicted day that is regarded as the flooding reference map. Although this flooding reference map is not the ground truth, the actual Landsat data classified using the same training samples and classifier can be an appropriate baseline to evaluate the effectiveness of these blending methods in flood mapping.
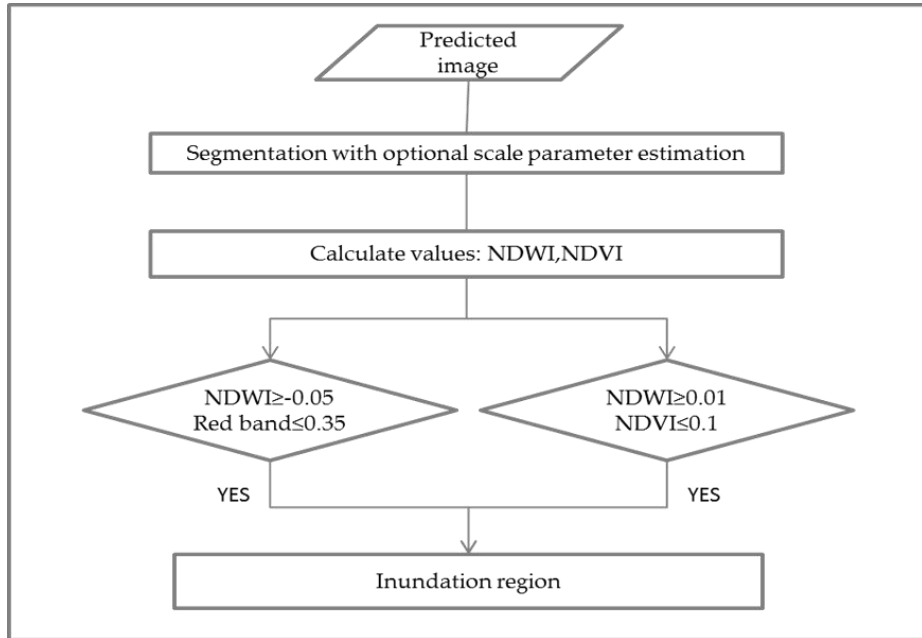
Figure 2 Flow chart of the decision tree approach for flood classification for the Predicted

image

Both visual interpretation and the error matrix will be applied to evaluate the eight inundation maps qualitatively and quantitatively. To focus on the flooded land, a mask was applied to remove the lake where FSDAF predict accurately. Error matrix (Congalton 1991) is used to assess the accuracy of all the inundation maps derived from the two groups of predictions according to the flooding reference map. Some commonly used statistical indices, such as user's accuracy (ua), producer's accuracy (pa), overall accuracy (oa), and kappa coefficient (kappa), are reported for accuracy assessment. In the end, the applicability of the methods will be

discussed for the two scenarios of flooding application based on their corresponding results in terms of both surface reflectance and flood maps.
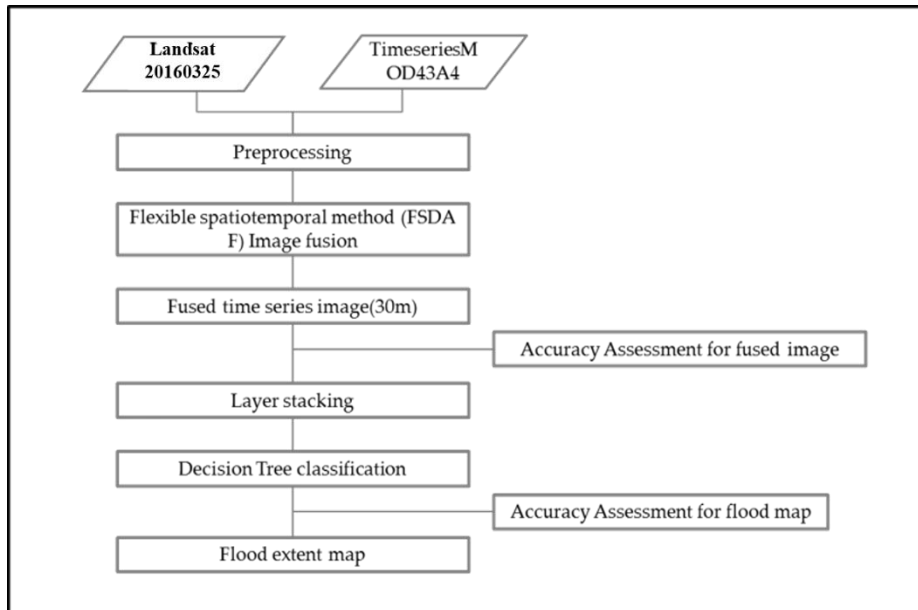
Figure 3 Flood inundation map flowchart for flood inundation map using Landsat and

MODIS image

3.2.4 Tumen river flood inundation simulation

The flood event from 29 to 31 August 2016 in Tumen river was a 100-year-frequency high storm rainfall event. According to the statistics obtained from United Nations Office on Humanitarian Affairs (OCHA)and it has 133 people were killed and 395 missing in North Hamkyung province in North Korea due to heavy rains and floods. More than 35,500 families have been

injured with 69% completely destroyed, and 8,000 public buildings have been damaged. It contains the city of Hunchun, Jilin, China and the adjacent areas where the River Tumen goes through. The storm event reappeared as the application case on the main hunchun of China. The average precipitation of the storm is as high as 648 mm in 36 h, with a 100-year frequency.

The flood event happened 29 to 31 August 2016, so the study using 29 August,2016 to 3 September,2016 to simulate the flood event time and flood inundation region. firstly, predicting flooding images through FSDAF on 29 August,2016 to 3 September,2016. Secondly, using DT mapping flood inundation and non-inundation. Next, to validate the simulation result, the study capture inundation scenario with the statistics obtained from United Nations Office on Humanitarian Affairs (OCHA). Finally, capture the flood event time and maximum inundation date and region.

When inundation occurs, this result map flood inundation region will full in map. the simulated inundation is generally consistent with the real scenario. Meanwhile, test the maximum inundation region and severely submerged spots and flood event occur and stop date during the event.

Chapter 4. Result and Discussions

4.1. Comparison of predicted image and original Landsat image land cover type change

4.1.1 Test with satellite images in heterogeneous landscape

Test with satellite images in heterogeneous landscape presents the Landsat-like image on March 25, 2016 predicted by the FSDAF methods. A zoom-in area was also used to highlight the difference between predicted images and the actual image. From the visual comparison, the images that the FSDAF methods predict are generally similar to the original Landsat image, suggesting that methods are able to capture the general temporal change in croplands from March 25, 2016 to August 16, 2016.

The predicted image of FSDAF is similar to the original image than are the images predicted spatial details, which can be seen from the zoom-in images. Particularly, comparing zoom-in are of the two original Landsat images, we can see that there is a parcel of paddy changed from non-vegetation to vegetation. Comparing the quantitative indices calculated using the input Landsat image from March 25, 2016 with the fused results,

value is RMSE=0.0301, AD=0.001, r=0.941 and SSIM=0.939. Can see that FSDAF methods have successfully added certain temporal change information to the input Landsat image to get the prediction on August 16, 2016. Through visually comparing the March 25, 2016 and predicted results via the FSDAF method, can see that the built-up details where no land cover type change happens. In contrast, the paddy and forest predicted by FSDAF is similar in shape to the true image, suggesting that FSDAF was able to produce a satisfactory simulation of the seasonal of objects that have under gone land cover type change.

Table 2 Accuracy assessment of FSDAF fusion methods applied to the study site with land cover type change. The units are reflectance (RMSE = Root Mean Square Error, r =correlation coefficient, AD= average difference from true reflectance, SSIM=structure similarity).

	RMSE	R	AD	SSIM
Band1	0.014	0.812	0.000	0.891
Band2	1.022	0.833	0.000	0.900
Band3	0.034	0.888	0.000	0.802
Band4	0.066	0.781	0.000	0.731
Band5	0.044	0.900	0.000	0.911
Band7	0.035	0.876	0.000	0.893

Table 2 shows the root mean square error (RMSE) and averaged difference (Diff) between the predictions and actual Landsat data in th e green, red, and NIR bands. The table shows several interesting char acteristics of the predicted results. First, all the Landsat image and Pr

edicted image on 29 August,2016 have negative invariable. Although i nvariably small, averaged differences are negative, indicating that the predicted values produced by FSDAF are lower than those in the actu al Landsat image. For all 6 bands, the fused results of FSDAF have smaller RMSE and higher r and SSIM (Table 2). The scatter plots of actual vs. predicted NIR band by the FSDAF methods also confirme d that values predicted by FSDAF are closer to the actual values. Th e two Landsat images were acquired within the early growing season of crops, so the NIR band experienced larger reflectance change than other bands. For the overall prediction bias, FSDAF methods can obta in nearly unbiased results for each band(|AD|b0.000).

4.1.2 Predicted surface reflectance on flood date

Table 3 indices of agreement between the classifications of the predicted images and classification of the original Landsat image using the same training data. Higher values of oa and kappa suggest a higher similarity between the classification map of a given predicted image and the original image. Classification of the FSDAF predicted image has the largest values oa and kappa. For individual classes, FSDAF also has higher agreement for all four of the classes. In particular, inundated land and water mapped in image predicted by FSDAF has retrieve pixels that have undergone land cover type change during the flooding event.

Table 3 Indices of agreement between the classifications of the predicted images and classification of the original Landsat image using the same training data.

	160816	160829	160830	160831	160901	160902	160903
User's accuracy	0.884	0.840	0.832	0.858	0.932	0.922	0.917
Producer's accuracy	0.887	0.871	0.889	0.862	0.912	0.901	0.900
Overall accuracy	0.878	0.838	0.864	0.854	0.901	0.921	0.898
Kappa	0.803	0.791	0.805	0.808	0.840	0.833	0.821

Figure 4 shows the predicted surface reflectance images from FSDAF, the first image is Landsat image (Figures 4(a)), and the following three images is in real-time prediction (Figures 4(b)–(e)). The image of the predicted date (Figure 4(c)) is shown as a reference at the bottom. As one of the input MODIS images of August 2016 has a small patch of inundation are impacted. When compared with all the other affected predictions, however, Figure 4(d) has been the most affected. For a better illustration of the different performances of all tests in the flooded area, especially on vegetation and residential land, two sub-regions including one freeway intersection and one community of Hunchun are highlighted (as marked in Figure 4(a)). All the real-time predictions show the abrupt drop in reflectance in the green space around the intersection, cannot delineate the exact flooding boundary. Figure 4(c) presented a much larger flooding area compared with the actual image. In the center of the city, all the predictions can roughly capture the flooding area, and linear objects such as roads are

clearly retained. However, Figure 4(d) is slightly better as it covers most of the flooded area as shown in the actual image. Such an advantage is also demonstrated in the case of wetland in the central eastern part, which was over-predicted in reflectance in other predictions.
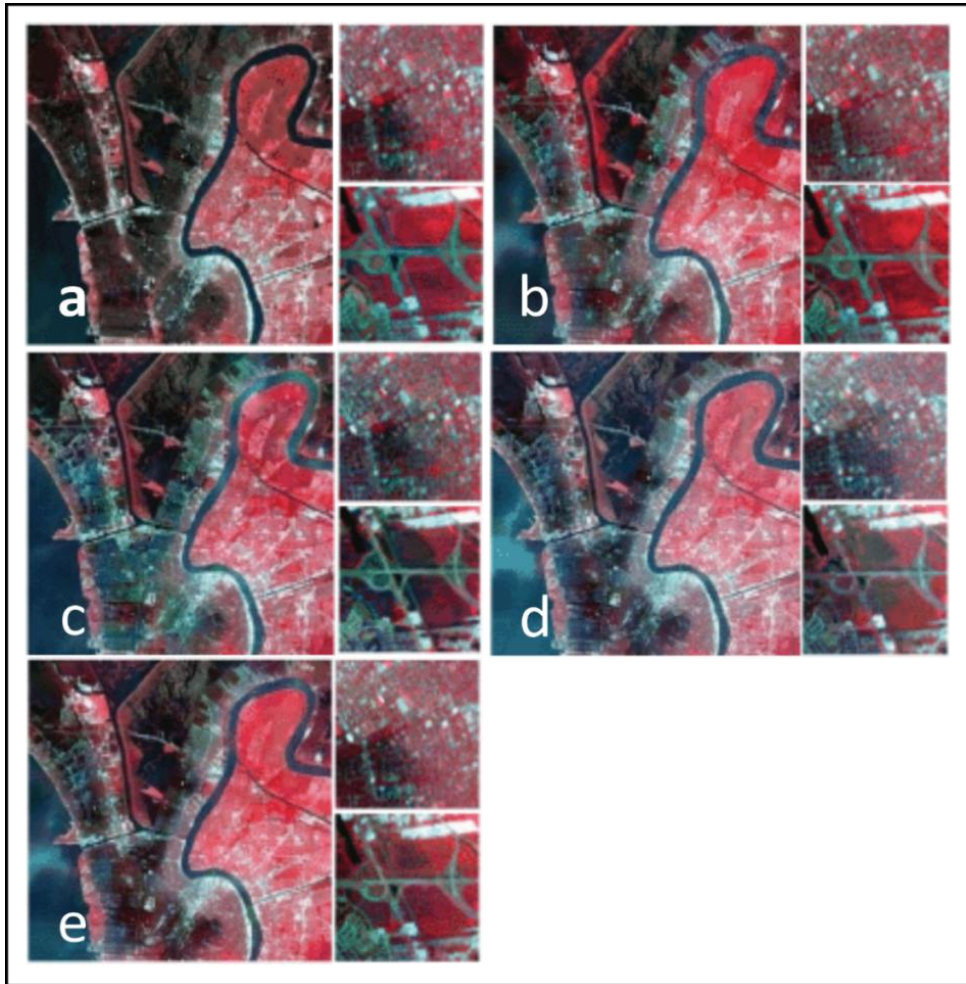
Figure 4 Five predicted images derived from FSDAF. The smaller images on Figure 4(a).

In the post-flooding prediction, as shown in Figure 4, compared with the even though all the predictions underestimated the flooding area near the freeway intersection, the extent and color in the central city match the reference image quite well. Such an outcome might result from the post-

event image of August 2016, where some floodwater remains in the city, but the flooding extent has shrunk considerably only leaving the ruins of buildings and trees as a trace.

Such an outcome might result from the post-event image of March 25, 2016, where some floodwater remains in the city, but the flooding extent has shrunk considerably only leaving the ruins of buildings and trees as a trace.

Table 4 RMSE and averaged difference (Diff) of the prediction value in the green, red, and
NIR bands.

	20160816	20160830	20160831	20160901	20160902	20160903
Green RMSE	0.026	0.025	0.023	0.024	0.020	0.023
Green Diff*	−0.016	−0.013	−0.013	−0.009	−0.004	−0.007
Red RMSE	0.029	0.030	0.026	0.030	0.051	0.022
Red Diff*	−0.014	−0.014	−0.011	−0.013	−0.001	−0.005
NIR RMSE	0.128	0.171	0.110	0.048	0.090	0.082
NIR Diff*	−0.060	−0.002	−0.031	−0.016	−0.003	−0.010

Note: *Diff is the averaged difference between observation value and the predicted value.

Table 4 shows the root mean square error (RMSE) and averaged difference (Diff) between the predictions and actual Landsat data in the green, red, and NIR bands. The table shows several interesting characteristics of the predicted results. First, all the Landsat image and Predicted image on 29 August,2016 have negative invariable. Although invariably small, averaged differences are negative, indicating that the

predicted values produced by FSDAF are lower than those in the actual Landsat image. Thus, the flooding extent or consequence which can be derived from these predicted images could be estimated high. Second, in the red and green bands, the methods have comparable performance while in the NIR band, because the RMSE of the NIR band in FSDAF results are stable at 0.04– 0.07 (less than twofold of the RMSE in the red and green bands). The larger prediction error in the NIR band is reasonable in flooding, as the reflectance of most surface objects (i.e. vegetation) in the NIR band is higher than that in the visible bands except water, which is close to zero. Therefore, during a flood, the value in the NIR band may show a very dramatic drop. Hence, the prediction error may be amplified by several times compared with other bands. In this respect, FSDAF results will be better in some flood mapping methods where the NIR band is used as an important index to extract the flooding area, such as NDWI (McFeeters 1996).

In the borders of agriculture regions, agriculture was always mixed with small proportion of other vegetation type or soil in the Landsat pixel for its moderate spatial resolution. The mixed pixels phenomenon was also presented in some small parcels in agriculture regions. Furthermore, terrain, small cloud and shadows influence on the flood inundation mapping would be weak by appending the fused time series data. Single Landsat spectral data might not contain enough information to identify flood inundation boundary misclassification in these regions and lead to not sure where is extent of flood damage. When fused time series data which contained more

flood information involved to the mapping to identifying.

4.2 Flood inundation mapping

The classification results of DT using the Landsat OLI and the composited spectral bands with time series MODIS were shown in Fig. 5. Two pairs of Landsat and MODIS images were applied to test the blending models in a flooding study of Tumen river basin in 20160829. Fig. 5 shows the flooding maps derived from the Landsat image and predicted image. In the following, these flooding maps will be named as were the predicted images from which they were derived for decision tree method. Blue represents flooding class while gray indicates non-flooding class. The differences between these flooding maps and the reference map are given in Fig. 5. In other words, they show an overestimation of flooding extent reality.

As shown in Figure 5, the red color (underestimation) is mainly distributed around the flood boundary on land, while the blue color (overestimation) appears to be near riverbanks and lake shores. The flooding maps derived from post-flooding predictions have larger grey areas, implying that these predicted maps match well with the reference map. Such a result is consistent with the former analysis of surface reflectance values. To further explore the capacity of these blending methods in flood mapping, the confusion matrix is computed. As shown in Table 3, the user's and

producer's accuracy of flooding area, overall accuracy, and kappa coefficient are listed for all seven predicted flooding maps. ua shows the proportion correctly identified as flooding class in the predicted map, so 1–ua is the commission error, which means the overestimation of flooding area in predicted maps. pa refers to the proportion of correctly classified flooding pixels in the reference map, so 1–pa is the omission error representing the underestimation of flooding area in predicted maps.
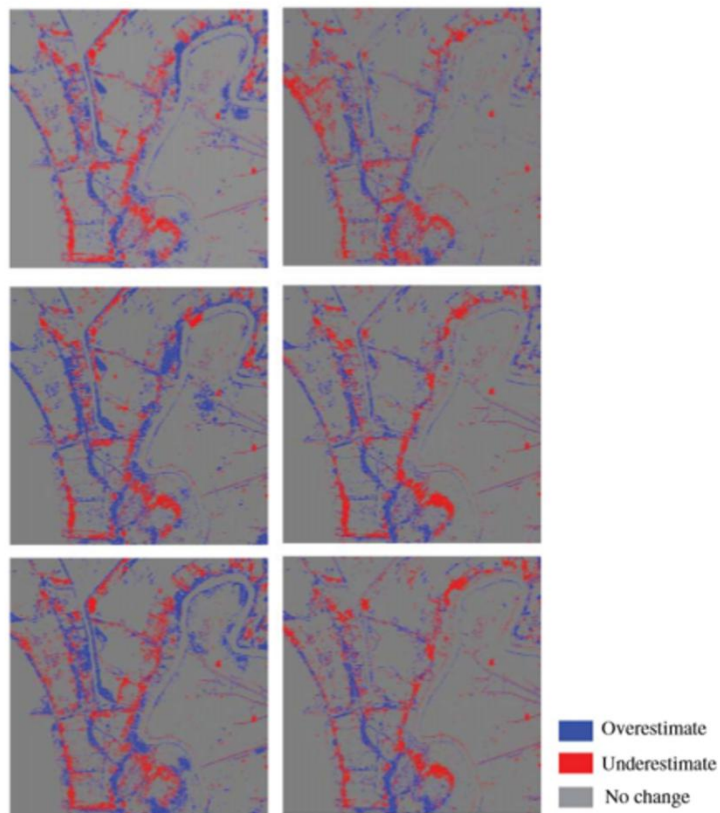

Figure 5 Differences between the seven predicted flooding maps and reference map.

Table 5 Accuracy of all flooding inundation maps derived from FSDAF prediction.

	160816	160829	160830	160831	160901	160902	160903
User's accuracy	0.884	0.840	0.832	0.858	0.932	0.922	0.917
Producer's accuracy	0.887	0.871	0.889	0.862	0.912	0.901	0.900
Overall accuracy	0.878	0.838	0.864	0.854	0.901	0.921	0.898
Kappa	0.803	0.791	0.805	0.808	0.840	0.833	0.821

Note*: User's accuracy and producer's accuracy are for flood area.

In Table 5, the highest ua in the scenarios of result, respectively, belongs to the flooding maps of 160829 to 160902, as 0.840, 0.832, 0.858, 0.893, 0.922. However, the highest values of pa in the scenario can be found in P_160901, P_160902 and P_160903, which are 0.912, 0.901 and 0.900, respectively. Landsat_160816, P_160816 and P_160831 have relatively lower ua and pa due to their low accuracy of the predicted images. The result indicates that no predicted map has both higher ua and pa. More specifically, a deviation exists in ua and pa in different scenarios. All the flooding maps derived from real-time predictions have a higher value of pa than ua (overestimation dominated). In contrast, all the flooding maps from post-flooding predictions show a higher ua than pa (underestimation dominated). Nevertheless, FSDAF is relatively more balanced in ua and pa when using images. This might be related to its obscure boundaries of flooding extent. oa and kappa indicate the general consistency between

predicted maps and reference map.

Results demonstrated the prediction of surface reflectance and flood mapping in real-time and post-flooding, respectively. It is relatively higher of Landsat 0.878 and kappa of 0.803 in the flood mapping using the real-time predictions while the OA and kappa of all the post-flooding predicted maps are approximately 0.8 and 0.9, respectively. The accuracy of flood maps in flooding groups is acceptable in this study. In the visual aspect, flood inundation could be identified effectively in each classification map based on the visual observation of the Landsat data. The mapping results of the main difference between two results were misclassification in the inundation region borders and small parcels in the interior of inundation region. This advantage in post-flooding mapping is mainly due to two factors. First, by including the post-flooding images, the predictions could make a better match with the actual Landsat image due to its additional spectral information on flooding. Hence, the accuracy of the post-flooding prediction has been generally enhanced. Second, even though the reflectance values predicted by FSDAF have higher errors, the differences in reflectance between flooding and non-flooding pixels are still large enough to be differentiated by the classifier. In other words, the error in predicted image using post-event imagery is not large enough to cause major misclassification in the flood mapping process.

This study still has some limitations that need to be addressed in the future. Considering the surface complexity and spectral characteristics of flooding, both image fusion is in adequate in accurately predicting the abrupt changes seen during urban flooding, resulting in either

overestimation or underestimation of flooding area near the flooding boundary. A more accurate flooding map might be obtained through further improving the blending model to enable it to provide better prediction of abrupt events. In addition, to improve the accuracy of flood-mapping results, such as rainfall, land-cover types, elevation, location of dams, the sewerage systems, fast river.

4.3 Tumen river flood event simulation

The study conducted the simulation to obtain the Tumen river flood maximum inundation region and severely submerged spots and flood event occur and stop date during the event. For further validation of the simulation result, we compare the result with the statistics obtained from United Nations Office on Humanitarian Affairs (OCHA). As shown in Figure 10 we know several facts: (1) the flood event was occur in 29 August,2016 end on 1 September,2016; (2) Similar accumulative pattern that flood inundation had maximum distribution on 31 August,2016 and the accumulative volume rises with the increasing rainfall duration on the same underlying surface with the rainfall until 1 September,2016 (3) From 2 September, 2016 flood inundation surface distribution area began smaller than last day. It can be observed from this figure that although the general pattern of simulated inundation is similar to actual flooding as represented by the surveyed data, there was capture of inundation areas in the locations where generated river network shifted from actual flow path. It was obvious as the flooding mainly

occurred due to the overflow of rivers. Also, it can be observed that the simulated inundation areas in upper part of the basin agree well with the surveyed one compared to the previous simulation. It can be observed from this figure that although the general pattern of simulated inundation is similar to actual flooding as represented by the surveyed data, there was capture of inundation areas in the locations where generated river network shifted from actual flow path. It was obvious as the flooding mainly occurred due to the overflow of rivers. Also, it can be observed that the simulated inundation areas in basin agree well with the surveyed one compared to the actual data, so the simulation result should be stable.
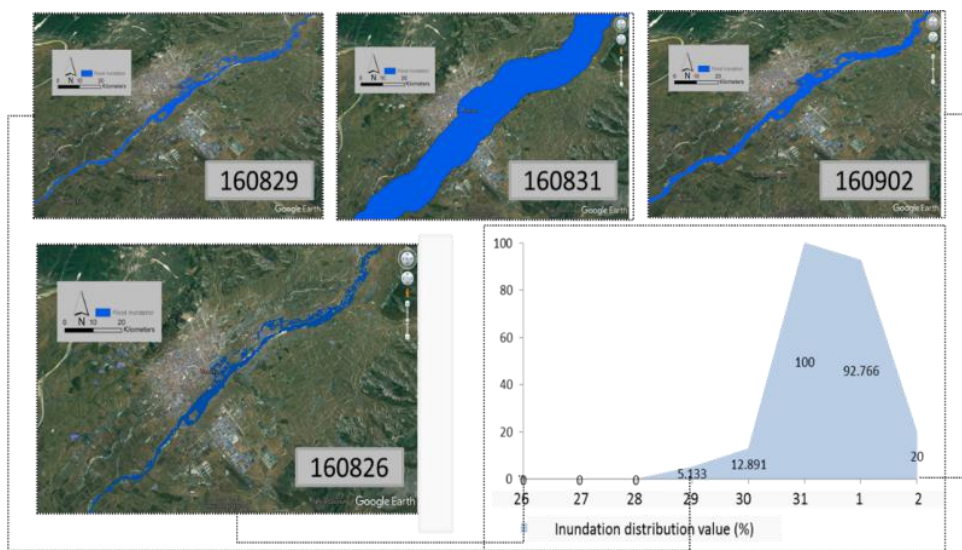

Figure 6 Simulated flood inundation map during 29 August to 3 September,2016

Chapter 5 Conclusions

Flooding is characterized by fast, abrupt changes in remote-sensing imagery. Flooding is more complicated due to its heterogeneity and spectral diversity. Studies of urban flooding require not only high-spatial resolution images to separate different land use types and delineate flooding extent, but also high-temporal resolution images to track the rapidly retreating flood process. Thus, FSDAF could make a significant contribution by blending different types of satellite imagery to improve spatial and temporal resolutions for flooding application. Landsat and MODIS images were applied to test the FSDAF models in a flooding study of Tumen river in China in 2016. Results demonstrated the differing capability of the models in the prediction of surface reflectance and flood mapping in scenarios of real-time and post-flooding, respectively.

First, by including the post-flooding images, the predictions could make a better match with the actual Landsat image due to its additional spectral information on flooding. Hence, the accuracy of the post-flooding prediction has been generally enhanced. Second, even though the reflectance values predicted by FSDAF have errors, the differences in reflectance between flooding and non-flooding pixels are still large enough to be differentiated by the DT classifier. In other words, the error in FSDAF prediction using post-event imagery is not large enough to cause major misclassification in the flood inundation mapping process. Therefore, these

FSDAF predictions could have an increased accuracy in flood mapping using post-flooding images.

This study still has some limitations that need to be addressed in the future. Considering the surface complexity and spectral characteristics of urban flooding, FSDAF are inadequate in accurately predicting the abrupt changes seen during urban flooding, resulting in either overestimation or underestimation of flooding area near the flooding boundary. A more accurate flooding map might be obtained through further improving the blending model to enable it to provide better prediction of abrupt events. In addition, to improve the accuracy of flood-mapping results, more information could be integrated into the classification process, such as rainfall, land-cover types, elevation, location of dams, the sewerage systems, and river gauge data for the city. Combining all these data with hydrologic models is helpful in detecting surface flooding and damage more accurately.

From simulate Tumen river flood event, (1) the flood event was happened in 29 August,2016 end on 1 September,2016; (2) Similar accumulative pattern that flood inundation had maximum distribution on 31 August,2016 and the accumulative volume rises with the increasing rainfall duration on the same underlying surface with the rainfall until 1 September,2016 (3) From 2 September,2016 flood inundation surface distribution area began smaller than last day. It can be observed from this figure that although the general pattern of simulated inundation is similar to actual flooding as represented by the surveyed data, there was capture of inundation areas in the locations where generated river network shifted from

actual flow path. Know when inundation occurs, this result map flood inundation region will full in map. Meanwhile, test the maximum inundation region and severely submerged spots and flood event occur and stop date during the event.

Although FSDAF show good performance in producing synthetic images for flood mapping, the spatial and temporal resolution of input observation data might affect the final results markedly. Specifically, for those flood events with few or even no cloud-free remote-sensing images, the blending result could be very poor. Thanks to their independence of weather and daylight, SAR images provide the potential for more accurate flood monitoring and assessment (Kuehn, Benz, and Hurley 2002). Recently, various methods have been developed to fuse SAR and optical images to take full advantage of SAR images in bad weather while improving its interpretation in heterogeneous areas (Xie and Keller 2006; Hong, Zhang, and Mercer 2009; Zhang 2009). Some researchers have also applied various blending methods in flood monitoring (Ramsey et al. 2009; Schumann et al. 2009; Bwangoy et al. 2010). Therefore, including SAR images in the blending framework for urban flooding studies will be the subject of our future work.

Bibliography

Assendorp, Dan. "Classification of pattern and process in small scale dynamic ecosystems; with cases in the Dutch coastal dunes." (2010).

Amorós López, Julia, et al. "Multitemporal fusion of Landsat/TM and ENVISAT/MERIS for crop monitoring." International journal of Applied earth observation and Geoinformation 23 (2013): 132-141.

Blaschke, Thomas. "Object based image analysis for remote sensing." ISPRS journal of photogrammetry and remote sensing 65.1 (2010): 2-16.

Bisquert, Mar, Agnès Bégué, and Michel Deshayes. "Object based delineation of homogeneous landscape units at regional scale based on MODIS time series." International Journal of Applied Earth Observation and Geoinformation 37 (2015): 72-82.

Chen, Gang, et al. "Object based change detection." International Journal of Remote Sensing 33.14 (2012): 4434-4457.

Conchedda, Giulia, Laurent Durieux, and Philippe Mayaux. An object based method for mapping and change analysis inmangrove ecosystems." ISPRS Journal of Photogrammetry and Remote Sensing 63.5 (2008): 578-589.

Coppin, Pol R., and Marvin E. Bauer. "Digital change detection in forest ecosystems with remote sensing imagery." Remote sensing

reviews 13.3-4 (1996): 207-234.

Devadas, R., R. J. Denham, and M. Pringle. "Support vector machine classification of object based data for crop mapping, using multi temporal landsat imagery." Int. Arch. Photogram. Remote Sens. Spat. Inf. Sci 39 (2012): 185-190.

Dronova, Iryna, Peng Gong, and Lin Wang. "Object based analysis and change detection of major wetland cover types and their classification uncertainty during the low water period at Poyang Lake, China." Remote Sensing of Environment 115.12 (2011): 3220-3236.

Dronova, Iryna, et al. "Mapping dynamic cover types in a large seasonally flooded wetland using extended principal component analysis and object based classification." Remote Sensing of Environment 158 (2015): 193-206.

Dronova, I., L. Wang, and P. Gong. "Object based analysis and change detection of the major wetland cover types during the low water period at Poyang Lake, PRC." AGU Fall Meeting Abstracts. 2010.

Dronova, Iryna, et al. "Landscape analysis of wetland plant functional types: The effects of image segmentation scale, vegetation classes and classification methods." Remote Sensing of Environment 127 (2012): 357-369.

Emelyanova, Irina V., et al. "Assessing the accuracy of blending Landsat MODIS surface reflectances in two landscapes with contrasting

spatial and temporal dynamics: A framework for algorithm selection." Remote Sensing of Environment 133 (2013): 193-209.

Frohn, R. C., et al. "Segmentation and object oriented classification of wetlands in a karst Florida landscape using multi season Landsat 7 ETM+ imagery." International Journal of Remote Sensing 32.5 (2011): 1471-1489.

Fu, Dongjie, et al. "An improved image fusion approach based on enhanced spatial and temporal the adaptive reflectance fusion model." Remote Sensing 5.12 (2013): 6346-6360.

Garrett, Henry E. "Factor analysis. An introduction and manual for the psychologi-st and social scientist." (1953): 227.

Gevaert, Caroline M., and F. Javier García Haro. "A comparison of STARFM and an unmixing based algorithm for Landsat and MODIS data fusion." Remote sensing of Environment 156 (2015): 34-44.

Grenier, Marcelle, et al. "An object based method to map wetland using RADARSAT 1 and Landsat ETM images: test case on two sites in Quebec, Canada." Canadian Journal of Remote Sensing 33.S1 (2007): S28-S45.

Gao, Feng, et al. "On the blending of the Landsat and MODIS surface reflectance: Predicting daily Landsat surface reflectance." IEEE Transactions on Geoscience and Remote sensing 44.8 (2006): 2207-2218.

Gong, Peng, and Bing Xu. "Remote sensing of forests over time." Remote sensing of forest environments. Springer US, 2003. 301-333.

Hess, Laura L., et al. "Dual season mapping of wetland inundation and

vegetation for the central Amazon basin." Remote sensing of environment 87.4 (2003): 404-428.

Heumann, Benjamin W. "An object based classification of mangroves using a hybrid decision tree Support vector machine approach." Remote Sensing 3.11 (2011): 2440-2460.

Hilker, Thomas, et al. "A new data fusion model for high spatial and temporal resolution mapping of forest disturbance based on Landsat and MODIS." Remote Sensing of Environment 113.8 (2009): 1613-1627.

Huang, Bo, and Huihui Song. "Spatiotemporal reflectance fusion via sparse representation." IEEE Transactions on Geoscience and Remote Sensing 50.10 (2012): 3707-3716.

Hilker, Thomas, et al. "A new data fusion model for high spatial and temporal resolution mapping of forest disturbance based on Landsat and MODIS." Remote Sensing of Environment 113.8 (2009): 1613-1627.

Ju, Junchang, and David P. Roy. "The availability of cloud free Landsat ETM+ dataover the conterminous United States and globally." Remote Sensing of Environment 112.3 (2008): 1196-1211.

Kim, Minho, et al. "Multi scale GEOBIA with very high spatial resolution digital aerial imagery: scale, texture and image objects." International Journal of Remote Sensing 32.10 (2011): 2825-2850.

Le Maire, Guerric, et al. "Mapping short rotation plantations at regional

scale using MODIS time series: Case of eucalyptplantations in Brazil." Remote Sensing of Environment 152 (2014): 136-149.

Lenssen, John, et al. "Control of plant species richness and zonation of functional groups along a freshwater flooding gradient." Oikos (1999): 523-534.

Liu, Desheng, and Shanshan Cai. "A spatial temporal modeling approach to reconstructing land cover change trajectoriesfrom multi temporal satellite imagery." Annals of the Association of American Geographers 102.6 (2012): 1329-1347.

Lu, Dengsheng, et al. "Change detection techniques." International journal of remote sensing 25.12 (2004): 2365-2401.

Mallinis, Giorgos, et al. "An object based approach for flood area delineation in a transboundary area using ENVISAT ASAR and LANDSAT TM data." International Journal of Digital Earth 6.sup2 (2013): 124-136.

Mas, JF. "Monitoring land cover changes: a comparison of change detection techniques." International journal of remote sensing 20.1 (1999): 139-152.

McCleary, A. L., K. A. Crews Meyer, and K. R. Young. "Refining forest classifications in the western Amazon using an intra annual multitemporal approach." International Journal of Remote Sensing 29.4 (2008): 991-1006.

Neeti, Neeti, and J. Ronald Eastman. "Novel approaches in extended

principal component analysis to compare spatio temporal patterns among multiple image time series." RemoteSensing of Environment 148 (2014): 84-96.

Villa, P., et al. "A multitemporal analysis of tsunami impact on coastal vegetation using remote sensing: a case study on Koh Phra Thong Island, Thailand." Natural hazards 64.1 (2012): 667-689.

Parrott, Lael, and Wayne S. Meyer. "Future landscapes: managing within complexity." Frontiers in Ecology and the Environment 10.7 (2012): 382-389.

Sakamoto, Toshihiro, et al. "Detecting temporal changes in the extent of annual flooding within the Cambodia and the Vietnamese Mekong Delta from MODIS time series imagery." Remote sensing of environment 109.3 (2007): 295-313.

Thompson, Jeffery A., and Brian G. Lees. "Applying object based segmentation in the temporal domain to characterise snow seasonality." ISPRS Journal of Photogrammetry and Remote Sensing 97 (2014): 98-110.

Vintrou, Elodie, et al. "Crop area mapping in West Africa using landscape stratification of MODIS time series and comparison with existing global land products." International Journal of Applied Earth Observation and Geoinformation 14.1 (2012): 83-93.

Xiaoxia, Sun, Zhang Jixian, and Liu Zhengjun. "A comparison of

object oriented and pixel based classification approachs using quickbird imagery." (2005).

Watson, Simon J., et al. "Land use change: incorporating the frequency, sequence, time span, and magnitude of changes into ecological research." Frontiers in Ecology and the Environment 12.4 (2014): 241-249.

Watts, Jennifer D., et al. "Improved classification of conservation tillage adoption using high temporal and synthetic satellite imagery." Remote Sensing of Environment 115.1 (2011): 66-75.

Weng, Qihao, Peng Fu, and Feng Gao. "Generating daily land surface temperature at Landsat resolution by fusing Landsat and MODIS data." Remote Sensing of Environment 145 (2014): 55-67.

Wu, Mingquan, et al. "Use of MODIS and Landsat time series data to generate highresolution temporal synthetic Landsat data using a spatial and temporal reflectance fusion model." Journal of Applied Remote Sensing 6.1 (2012): 063507-1.

Yu, Le, Yichuan Shi, and Peng Gong. "Land cover mapping and data availability incritical terrestrial ecoregions: A global perspective with Landsat thematic mapper and enhanced thematic mapper plus data." Biological Conservation 190 (2015): 34-42.

Zhukov, Boris, et al. "Unmixing based multisensor multiresolution image fusion." IEEE Transactions on Geoscience andRemote Sensing 37.3 (1999): 1212-1226.

Zhu, Xiaolin, et al. "An enhanced spatial and temporal adaptive

reflectance fusion model for complex heterogeneous regions." Remote Sensing of Environment 114.11 (2010): 2610-2623.

Zurita Milla, Raul, Jan GPW Clevers, and Michael E. Schaepman. "Unmixingbased Landsat TM and MERIS FR data fusion." IEEE Geoscience and Remote Sensing Letters 5.3 (2008): 453-457.

Abstract (Korean)

　　최근 들어 지구온난화 및 이상기후 등 기상이변으로 인해 빈번히 발생하고 있는 이상 홍수에 대한 피해가 급증하고 있다. 또한 기후변화에 따른 강우량의 증가와 집중호우로 인한 홍수 피해는 지속적으로 증가할 것으로 예상됨에 따라 홍수 침범 지역 매핑 연구가 활발히 진행되고 있다.

　　시간해상도와 공간해상도가 높은 영상 자료는 효과적인 홍수 침범 지역 매핑을 위해서 필수적이다. 하지만 단일 센서를 통한 영상은 공간해상도와 시간해상도가 높은 자료를 동시에 제공할 수 없는 한계점이 있다. 최근에는 위성 영상의 공간적 해상도를 높이고 시간해상도를 보완하기 위해서 시공간 융합 연구가 진행되고 있다. 그 중에서도 FSDAF(Flexible spatiotemporal data fusion) 방법론은 위성 영상의 각 밴드를 융합 하는 방법으로 적절한 것으로 나타났다.

　　본 연구에서는 FSDAF 융합 기법을 활용하여 홍수로 영향이 많은 중국 두만강 하류를 테스트베드로 선정하여, MODIS와 Landsat 영상을 융합 후 검증을 실시하였으며 홍수침범지역 모니터링에서의 활용가능성을 제시하였다. 본 연구의 방법을 적용하여 2016년 두만강 하류에서 발생한 홍수의 경우와 비교한 결과, 유사한 홍수 범람 지도를 획득 할 수 있었으며, 실제 홍수 범람지역에서의 발생한 날짜와 종료된 날짜 예측이 가능하며, 홍수 범람 지역의 면적은 실제 홍수 범람지역에서의 면적보다 더 크게 나타나는 특성을 파악할 수 있었다.

　　본 연구에서 활용된 FSDAF 시공간 융합 기법은 픽셀 기반의 융합기법으로 다양한 공간 스케일의 영상과도 융합 가능할 것이며 다양한 홍수 관련 연구에 활용될 것으로 기대된다.